Journal of Nanotechnology & Advanced Materials
An International Journal

http://dx.doi.org/10.18576/jnam/050105

Effect of Calcination Temperature on Magnetic and Electrical Properties of $BiFeO_3$ Nanoparticles Prepared By Sol-Gel Method

E. M. M. Ibrahim[1], G. Farghal[1], Mai M. Khalaf[2], Hany M. Abd El-Lateef[2]*

1 Physics Department, Faculty of Science, Sohag University, Sohag-82524, Egypt
2 Chemistry Department, Faculty of Science, Sohag University, Sohag-82524, Egypt

Received: 1 Sep. 2016, Revised: 2 Nov. 2016, Accepted: 11 Nov. 2016.
Published online: 1 Jan. 2017.

Abstract: In this work, a $BiFeO_3$ nanoparticle was synthesized by sol–gel method followed by calcination at different temperature 300, 400 and 500 ˚C. Effect of calcination temperature on the structure, morphology, electrical and magnetic properties was studied by using x-ray diffraction, scanning electron microscopy, electrical conductivity measurements and vibrating sample magnetometer, respectively. Structural analysis revealed a typical rhombohedral phase of the prepared $BiFeO_3$ nanoparticles. Scanning electron microscope investigations show that the materials are mesoporous nature with average particle size ~ (52) nm. The magnetic measurement shows significant enhancement of the ferromagnetism with the increasing of the calcination temperature which may be mainly attributed to the crystallinity improvement and the change of the oxygen vacancies content. The DC electrical resistivity measurement was carried out by the two-probe method. The temperature dependence of resistivity behavior shows typical semiconductor features for the synthesized nanoparticles.

Keywords: $BiFeO_3$ nanoparticles; magnetic properties; electrical properties; sol-gel; antiferromagnetic.

1 Introduction

Bismuth ferrite ($BiFeO_3$), shortly denoted as BFO, has attracted considerable attention in recent years because of its multiferroic characteristics, ferromagnetism and ferroelectricity [1-5]. It has a wide range of applications such as magnetic data storage, logic devices, spintronic devices, and sensors [6–9]. The unit cell of $BiFeO_3$ can be described by a) hexagonal $[111]_{hex}$ ||, b) stable perovskite rhombohedral $[111]_{rh}$ || at room temperature, and c) pseudo-cubic structure $[001]_{pc}$ at 1204K as well as it undergoes a structural transition to orthorhombic phase near 1098K [10-14]. Magnetically, bulk BFO has antiferromagnetic characteristics below a Néel temperature, T_N~ 643 K [15]. Magnetization arises in BFO due to exchange interaction of localized electrons in partially filled d or f shells, but the poor magnetic property is due to i) Fe-O-Fe Dzyaloshinskii-Moriya exchange interactions on B-site (Fe) which gives rise to weak antiferromagnetic ordering and ii) a magnetic cycloidal spin structure with a long periodicity of 62 nm [10 and 16]. To overcome the limitations and to maximize the BFO utility, the magnetic properties of this type of ferrite should be enhanced. In order to enhance the magnetic properties of BFO nanostructured samples, the following four characteristics should be achieved: i) enhancement of surface-induced magnetization resulted from uncompensated spins, ii) an increase of spin canting due to lattice strain in nano-sized scale, iii) incomplete spiral of magnetic order in particles less than ~62 nm, iv) existence of oxygen deficiency that leads to Fe^{2+} ions and grow of magnetic Fe_2O_3 as an impurity [17 and 18].

Many, researchers have attempted to synthesis nanostructured $BiFeO_3$, such as spherical, nanorods, nanowires, and plates with different methods [18, 19-25]. Several techniques have been utilized to prepare $BiFeO_3$ nanostructures, ball-milling technique, co-precipitation, polymeric assisted rout, hydrothermal, reverse micelles etc. Choosing proper synthesis techniques play an important role in controlling the size and surface area and hence the properties of materials.

*Corresponding author e-mail: gehad.farghal@gmail.com

Among all used techniques, the sol-gel method has many advantages such as the use of low temperature, low cost, simplicity, energy saving, relatively low impurity content resulting from the easy formation of bismutite phase during calcination and uniform-sized BFO nanoparticles [10, 26-29]. This process is superior to the traditional Pechini's method [30].

In this work, $BiFeO_3$ nanostructures have been synthesized using the sol-gel method. The effect of calcination temperature on the structural, morphological, magnetic and electrical properties has been studied. Other research groups synthesized various $BiFeO_3$ nanostructures using the sol-gel method but to the best of our knowledge, study of the effect of calcination temperature on their properties was not carried out.

2 Subjects and Methods

2.1 Materials

The raw materials used in the process were highly pure, bithmuth nitrate [Bi $(NO_3)_3.5H_2O$] (99% assay) as precursor of Bi, iron nitrate [Fe $(NO_3)_3{\cdot}9H_2O$] (99% assay), citric acid (99% assay). All the chemicals were of analytical grade, commercially available, supplied by Shanghai Chemical Reagent Ltd (PR China) and used without further purification.

2.2 Preparation method

$BiFeO_3$ nanoparticles were synthesized using sol-gel reaction with calcination at different temperatures, 300˚C, 400˚C and 500˚C. Bismuth nitrate [Bi $(NO_3)_3.5H_2O$] (0.05 mol), iron nitrate [Fe $(NO_3)_3.9H_2O$] (0.1 mol), citric acid (0.23 mol) were weighed and dissolved in double distilled water. Afterward, the mixture was stirred for 15 min to obtain a homogeneous solution. Then, an amount of aqueous ammonia NH_3 (pH=8-9) was added to the solution with stirring for one hour at 90˚C. After that, the mixture was aged for 24 hours. The beaker with the solid deposit was placed in the oven at 100˚C. Combustion of the resultant gel at 180˚C was carried out with an evolution of large amounts of gaseous products and given dark gray deposit with a ramified structure. Then the burnt solid deposit was grinded and was followed by calcination in air at 300˚C, 400˚C and 500˚C for 3 hours, to obtain well crystallized bismuth ferrites nanoparticles. After the calcination process, the internal structure of the samples was characterized by the x-ray diffraction (XRD) (Brucker Axs-D8 Advance diffractometer with CuK_α radiation at λ = 1.5406 Å). The samples morphology was investigated using scanning electron microscope (SEM) model: Quanta FEG250. The magnetic properties of the samples were measured by using a vibrating sample magnetometer VSM 9600 LDJ. The electrical properties were studied by measuring the electrical resistivity as a function of temperature within a temperature range 443 – 723K using the two-prop technique.

3 Results

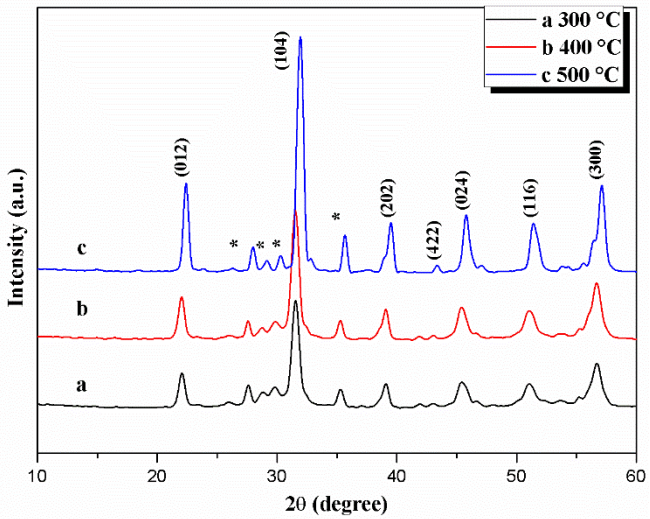

Figure.1. XRD of BFO samples at a) 300˚C, b) 400˚C, and c) 500˚C.

Fig. 1. Shows the XRD patterns of the BFO nanoparticles (NPs) synthesized at different calcination temperatures. The diffraction peaks characterize rhombohedral structure of $BiFeO_3$ belongs to R3c space group. Generally, the calcination process at different temperature doesn't alter the rhombohedral phase of the prepared samples. However, the peaks intensities increase as the calcination temperature increases indicating that the grains grow with enhancement of crystallinity [31]. Note that, four peaks (denoted by * on the XRD patterns) correspond to $Bi_2Fo_4O_9$ phase were observed on the XRD patterns and their intensities are nearly constant for all the samples of different calcination temperature. Therefore, based on the XRD results, the prepared samples are not monophase materials but consist of a mixture of two Bi ferrite phases with domination of the $BiFeO_3$ phase. The appearance of $Bi_2Fo_4O_9$ phase is in consistent with many other publications [32-36] and can be attributed to the large bismuth loss at higher temperatures due to, high volatility of Bi_2O_3 which leads to a formation of bismuth deficient phase $Bi_2Fe_4O_9$. Obviously, we can observe that the XRD pattern of the sample calcined at 500 ˚C is the smoothest with less noise compared to those of the samples calcined at lower temperatures. This indicates that the calcination temperature 500 ˚C is more appropriate for maximizing the Bi_2O_3 reaction with Fe_2O_3 and produces a highly crystalline BFO nanostructured [31]. The average crystallite size (D_{XRD}) of the synthesized NPs was calculated using the Debye-Scherer equation [37]: ($D_{XRD}=0.9\lambda/\beta\cos\theta$) where β is the full width at half maximum (FWHM) of the most intense peak, λ is the Cu target wavelength (1.5406Å) and θ is the glancing angle. The grain size calculated from Scherrer equation are equal to 13, 13.2 and 14 nm for samples calcined at 300˚C, 400˚C and 500˚C, respectively.

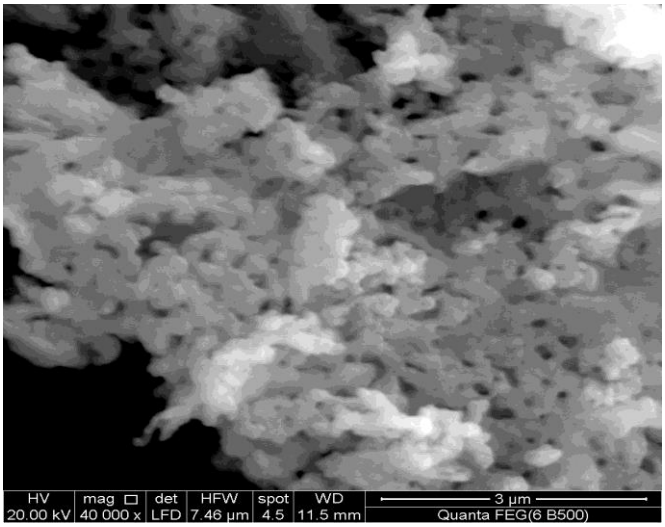

Figure. 2. SEM Scanning Electron Microscopy of BFO NPs at 500˚C.

Fig. 2 shows the Scanning Electron Microscopy SEM of BFO NPs annealed at 500˚C for 3 h. SEM analyses show that the materials are mesoporous in nature with average particle size D_{SEM}~ (52) nm. Note that, the value of D_{SEM} is higher than the crystallite size determined from the XRD data (D_{XRD}) because the particle consists of several crystallites [38].

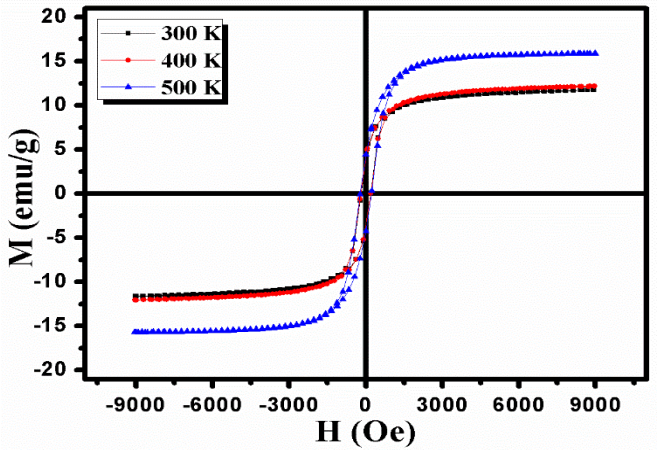

Figure. 3. Room temperature hysteresis (M-H) loops of samples at 300˚C, 400˚C and 500˚C.

For studying the magnetic properties of the materials at hand, the magnetic field dependence of magnetization was measured at room temperature over a magnetic field of ±1 T. The M–H loops are illustrated in Fig. 3. The data indicate a small hysteresis confirming that the samples are ferromagnetic in nature. This behavior is in contrary to that of bulk bismuth ferrite which is a typical antiferromagnetic system at room temperature. Several models were introduced to explain the ferromagnetic features of the nano-scaled BFO alloys [10, 39-44]. The reasons can be summarized as the following: a) according to Néel's theory, small antiferromagnetic NPs exhibit measurable magnetization due to incomplete spin compensation between two spin sublattices and the existence of defects such as O vacancies, b) the larger surface to volume ratio of the NPs enhances the contribution of uncompensated surface spin, c) the spin cycloid structure of $BiFeO_3$ is suppressed in the particles of size below 62nm due to grain size confinement effect [18,39-41,45,46]. The increase of saturation magnetization as the calcination temperature increases can be attributed to a) creation of oxygen vacancies which lead to the existence of Fe^{3+} [41, 33-36, 47-50], b) conversion of Fe^{3+} cations to Fe^{4+} cations [51], and c) the decrease of the spin spiral structure.

The saturation magnetization (M_s), remanent magnetization (M_r) and coercivity (H_c) were determined and tabulated in Table 1. As seen, the values of Ms, M_r, and H_c increase as the calcination temperature increases. The coercivity variation with the calcination temperature can be explained in the light of the associated change in the particle size. In ferromagnetic materials, where the particle size is larger than the domain wall width, the magnetization reversal depends on the domain wall motion. Therefore, increasing the grain size is expected to decrease H_c due to a decrease of the grain boundaries at which the domain walls are pinned where pinning is the main source of the coercivity [52]. Consequently, increasing the grain size is expected to decrease the pinning sites and to decrease H_c. However, below a certain grain size D_{Cr}, coherent magnetization reversal of a single magnetic domain become feasible and H_c increases as the grain size increases. For our materials, the case of grain size lower than D_{cr} is realized, therefore, H_c increases with the calcination temperature due to the associated increase in the grain size.

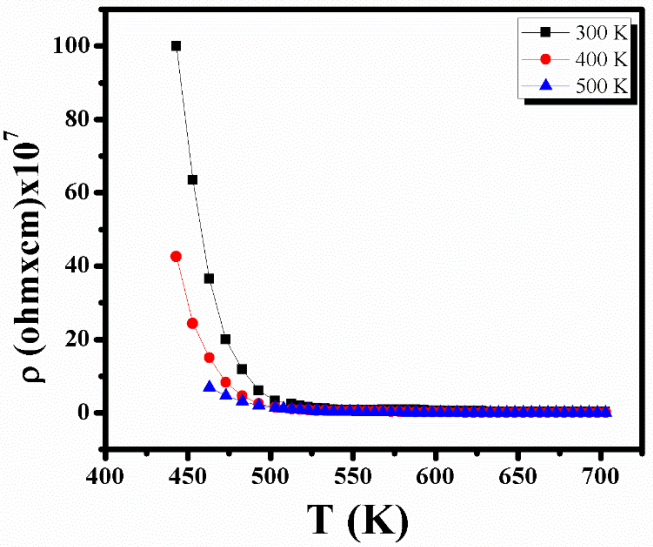

Figure. 4. Effect of calcination temperature on the resistivity of $BiFeO_3$ NPs at 300˚C, 400˚C and 500˚C.

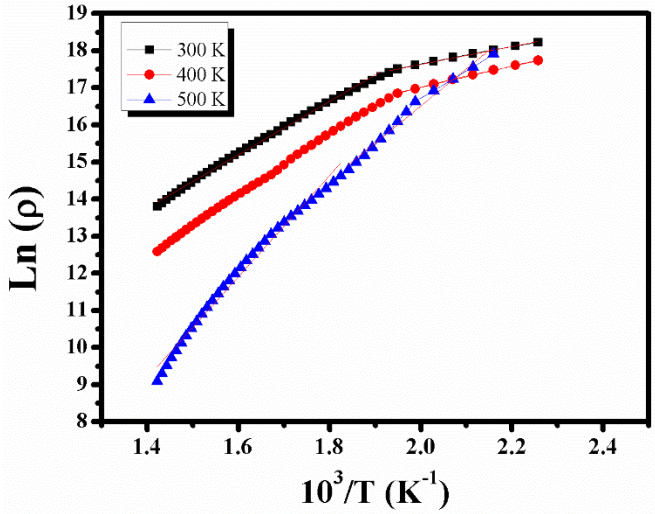

Figure. 5. DC electrical resistivity dependent on calcination temperature for $BiFeO_3$ NPs at 300˚C, 400˚C and 500˚C.

Fig. 4. Shows the DC-electrical resistivity of $BiFeO_3$ samples calcined at different calcination temperature 300˚C, 400˚C and 500˚C. Obviously, the resistivity (ρ) decreases drastically with the increase of temperature (T) showing a typical semiconductor behavior. The isothermal resistivity values measured at 460 K (ρ_{460K}), as an example, are 999.1, 426.1 and 68.8 MΩ.cm for samples calcined at 300, 400 and 500˚C, respectively. This means that the NPs resistivity is reduced by one order of magnitude by increasing the calcination temperature. The ρ-T plots fit well with the well-known Arrhenius equation:

$\rho = \rho_0 \exp(E_a/k_BT)$ where ρ_0 is the pre-experimental factor representing the temperature independent resistivity, E_a is the activation energy and k_B is the Boltzmann constant [53]. The linear behavior of Ln (ρ)−1000/T plots presented in Fig. 5 confirm that the conduction mechanism in the sample is thermally activated and fit well with the Arrhenius equation. As seen, each plot consists of two linear portions with different slopes and activation energies. This behavior indicates that the electrical conduction in the sample passes through two mechanisms upon the increase of temperature. The transition between the electrical mechanisms appears at certain temperature T_σ which was found to decrease with the calcination temperature as seen from the values depicted in Table 1. The activation energies at low (T≤Ts) and high (T≥Ts) temperature ranges of measurement (E_{Low} and E_{High}, respectively) were calculated from the Ln (ρ) − 1000/T plots and their values have been tabulated in Table 1. As seen, E_{Low} is lower than the E_{High} for the same sample. The data are comparable to those reported by Yao et al. [54] who attribute the activation energy E_{Low} to the ionic conduction mechanism caused by the oxygen vacancies in perovskite type ferroelectric oxides. However, E_{High} corresponds to the energy band mechanism or hopping mechanism of localized charge carriers [53 and 55].

Table. 1: Comparison of various parameters of $BiFeO_3$ samples calcined at 300˚C, 400˚C and 500˚C.

Calcination temperature	M_r (emu/g)	M_s (emu/g)	H_c (O_e)	E_{Low}	E_{High}	T_σ(K)
300˚C	3.71	11.74,	194.2	0.2	0.61	520.2
400˚C	3.80	12.13	199.1	0.26	0.7	512.8
500˚C	4.41	15.87	224.5	0.64	1.08	502.5

4 Conclusion

Bismuth ferrite NPs ($BiFeO_3$) are successfully synthesized by Sol-Gel method. Structural analysis revealed rhombohedral phase formation with crystallite size varying from 13 to 14 nm. The magnetization of bismuth ferrite NPs was enhanced by increasing the calcination temperature which was attributed mainly to the increase of oxygen vacancies, conversion of Fe^{3+} cations to Fe^{4+} cations and suppression of spin spiral structure. Temperature-dependent DC electrical resistivity (ρ) decreases drastically with the increase of temperature (T) showing a typical semiconductor behavior. However, two

mechanisms are involved in the electrical conduction, the ionic conduction mechanism at low temperature range and band-band or hopping conduction mechanism at the high temperature range of measurements.

References

[1] M. Mahesh Kumar, V. R. Palkar, K. Srinivas, S. V. Suryanarayana, *Appl. Phys. Lett*. **76**, 2764-2766, (2000).

[2] J. Wang, *Science*. **299**, 1719-1722, (2003).

[3] J. Wang, H. Zheng, Z. Ma, S. Prasertchoung, M. Wuttig, R. Droopad, J. Yu, K. Eisenheiser, R. Ramesh, *Appl. Phys. Lett*. **85**, 2574, (2004).

[4] Y. P. Wang, G. L. Yuan, X. Y. Chen, J.-M. Liu, Z. G. Liu, *J. Phys. D: Appl. Phys*. **39**, 2019, (2006).

[5] J. Wang, J.B. Neaton, H. Zheng, V. Nagarajan, S.B. Ogale, B. Liu, D. Viehland, V. Vaithyanathan, D.G. Schlom, U.V. Waghmare, N.A. Spaldin, K.M. Rabe, M. Wuttig, R. Ramesh, *Science*. **299**, 1719, (2003).

[6] T.Kimura, S. Kawamoto, I. Yamada, M. Azuma, M. Takano, Y. Tokura, *Phys. Rev*. **B 67**, 180401, (2003).

[7] N. Hur, S. Park, P. A. Sharma, J. S. Ahn, S. Guha, S. W. Cheong, *Nature*. **429**, 392–395, (2004).

[8] W. Eerenstein, N. D. Mathur, J. F. *Scott, Nature*. **442**, 759–765, (2006).

[9] SA Ahmed, EMM Ibrahim, SA Saleh, *Applied Physics A* **85**, 177-184, (2006)

[10] F. Majid, S. T. Mirza, S. Riaz, S. Naseem, *Materials Today: Proceedings*. **2**, 5293 – 5297, (2015).

[11] S.N. Tripathy, B. G. Mishra, M. M. Shirolkar, S. Sen, S. R. Das, D. B. Janes, D. K. Pradhan, *Mater. Chem. Phys*. **141**, 423-431, (2013).

[12] T. Ahmed, A. Vorobiev, S. Gevorgian, *Thin Solid Films*, **520**, 4470-4474, (2012).

[13] X. Chen, H. Zhang, K. Ruan, W. Shi, *J. Alloy Compd*. **529**, 1-108, (2012).

[14] S.A. Saleh, S.M. Khalil, E.M.M. Ibrahim, *Superconductor Science and Technology* **20**, 372, (2007)

[15] J. R. Teague, R. Gerson, W. J. James, *Solid State Commun*. **8**, 1073–1074, (1970).

[16] Y. P. Wang, L. Zhou, M.F. Zhang, X.Y. Chen, J.-M. Liu, Z.G. Liu, *Appl. Phys. Lett*. **84**, 1731-1733, (2004).

[17] S. Chauhan, M. Kumar, S Chhoker, S.C. Katyal, *J. Alloy Compd*. **666**, 454-467, (2016).

[18] T.J. Park, G.C. Papaefthymiou, A.J. Viescas, A.R. Moodenbaugh, S.S. Wong, *Nano Lett*. **7**, 766-772, (2007).

[19] S.-Z. Lu, X. Qi, J. Am. *Ceram. Soc*. **97**, 2185-2194, (2014).

[20] Pavana S.V. Mocherla, C. Karthik, R. Ubic, M.S. Ramachandra Rao, C. Sudakar, *Appl. Phys. Lett*. **103**, 022910, (2013).

[21] Pittala Suresh, S. Srinath, *J. Alloys Compd*. **649**, 843-850, (2015).

[22] J.-P. Zhou, R.-J. Xiao, Y.-X. Zhan0g, Z. Shi, G.-Q. Zhu, *J. Mater. Chem*. **C 3**, 6924-6931, (2015).

[23] B. Liu, B. Hu, Z. Du, *Chem. Commun*. **47**, 8166-8168, (2011).

[24] S. Bharathkumar, M. Sakar, K. Rohith Vinod, S. Balakumar, *Phys. Chem. Chem. Phys*. **17**, 17745-17754, (2015).

[25] X. Yang, G. Xu, Z. Ren, X. Wei, C. Chao, S. Gong, G. Shen, G. Han, *Cryst. Eng. Comm*. **16**, 4176-4182, (2014).

[26] J. Wei, D. Xue, *Materials Research Bulletin*. **43**, 3368–3373, (2008).

[27] S. Godaraa, N. Sinhaa, G. Raya, B Kumar, *Journal of Asian Ceramic Societies*. **2**, 416–421, (2014).

[28] X. Wang, Y. Zhang, Z. Wu, *Mater Lett*. **8**, 64–486, (2010).

[29] R.R. Sinha, S.K. Sinha, M. Mursaleen, S. Bera, J. Mahta, A. Kumar, *Journal of Applied Physics* **7**, 44-47, (2015).

[30] M.P. Pechini, *US Patent*. **3**, 330-697, (1967).

[31] M. Sakar, S. Balakumar, P. Saravanan, S.N. Jaisankar, *Materials Research Bulletin*. **48** 2878–2885, (2013).

[32] Y. Wang, Q. Jiang, H. He, C. W. *Nan, Appl. Phys. Lett*. **88**, 142503, (2006).

[33] Z. Quan, H. Hu, S. Xu, W. Liu, G. Fang, M. Li, X. Zhao, *J. Sol-Gel Sci. Technol*. **48**, 261-266, (2008).

[34] H. Zhang, X. Chen, T. Wang, F. Wang, W. Shi, *J. Alloys Compd*. **500**, 46-48, (2010).

[35] J.H. Xu, H. Ke, D. C. Jia, W. Wang, Y. Zhou, *J. Alloys Compd*. **472**, 473-477, (2009).

[36] V. Zelezny, D. Chvostova, L. Pajasova, I. Vrejoiu, M. Alexe, *Appl. Phys*. **100(4)**, 1217-1220, (2010).

[37] P. Debye, Zerstreuung von röntgenstrahlen, *Ann. Phys*. **351**, 809-823, (1915).

[38] M.M. Ibrahim, E.M.M. Ibrahim, S.A. Saleh, A.M. Abdel Hakeem, *Journal of Alloys and Compounds*. **429**, 19-24, (2007).

[39] G. Dhir, P. Uniyal, N. K. Verma *J. Magn. Magn. Mater*. **394**, 372–378, (2015).

[40] S. Basu, M.Pal, D.Chakravorty, *J. Magn. Magn. Mater*. **320**, 3361–3365, (2008).

[41] A. Manzoor, A. M. Afzal, M. Umair, A. Ali, M. Rizwan, M. Z. Yaqoob, , *J. Magn. Magn. Mater*. **393**, 269–272, (2015).

[42] A. M. Afzal, M.Umair, G.Dastgeer, M.Rizwan, M.Z.Yaqoob, R.Rashid, H.S.Munir, *J. Magn. Magn. Mater*. **399**, 77–80, (2016).

[43] Fabian E. N. Ramirez, Gabriel A. C. Pasca, Jose A. Souza, *Physics Letters*. **A 379**, 1549–1553, (2015).

[44] E.M.M. Ibrahim, Silke Hampel, Raghunandan Kamsanipally, Juergen Thomas, Kati Erdmann, Susanne Fuessel, Christine Taeschner, Vyacheslav O. Khavrus, Thomas Gemming, Albrecht Leonhardt, Bernd Buechner, *Carbon*. **63**, 358-366, (2013).

[45] S. M. Selbach, T. Tybell, M. A. Einarsrud, etal., *Chem. Mater*.**19(26)**, 6478-6484, (2007).

[46] R. Mazumdar, P. S. Devi, D. Bhattacharya, P. Choudhury, A. Sen, *Appl. Phys. Lett*. **91**, 062510, (2007).

[47] S. M. H. Shah, A. Akbar, S. Riaz, S. Atiq, S. Naseem, *IEEE Trans. Magn*. **50**, 2201004, (2014).

[48] S. Riaz, S.M.H. Shah, A. Akbar, S. Atiq, S. Naseem, *J. Sol-Gel Sci. Technol*. **74**, 329–339, (2015).

[49] F. Majid, S. Riaz and S. Naseem, *J. Sol-Gel Sci. Technol*. **74**, 310–319, (2015).

[50] S. Riaz, F. Majid, S. M. H. Shah, S. Naseem, *Indian J.Phys*. **88(10)**, 1037–1044, (2014).

[51] S. Chauhan, M. Kumar, S. Chhoker, SC. Katyal, H. Singh, M. Jewariya, KL. Yadav, *Solid State Commun*. **152**, 525–529, (2013).

[52] G. Herzer, *J. Magn. Magn. Mater*. **112(1–3),** 258–262, (1992).

[53] E. M. M. Ibrahim, *Appl. Phys*. **A 89**, 203–208, (2007).

[54] Z. Yao, H. Li, M. Ma, R. Chu, Z. Xu, J. Hao, G. Li, *Ceramics International*. **42**, 5391–5396, (2016).

[55] R. Das, S. Sharma, K. Mandal, *J. Magn. Magn. Mater*. **401**, 129–137, (2016).